npj | materials degradation

Article

Published in partnership with CSCP and USTB

https://doi.org/10.1038/s41529-026-00752-5

Speciation and radiation stability of Cr and *Ln* "Grey-Phases" within Cr-doped (*Ln*,U)O_2 spent fuel model materials

Daniil Shirokiy[1] ✉, Andrey Bukaemskiy[1], Maximilian Henkes[1], Elena F. Bazarkina[2,3], Christoph Hennig[2,3], Andrew Ryan[1,4], Martina Klinkenberg[1], Murat Güngör[1], Mara McCleary[1], Julien Marquardt[5], Andrew Fitch[6], Kristina O. Kvashnina[2,3], Dirk Bosbach[1] & Gabriel L. Murphy[1] ✉

Cr-doped UO_2 fuels are increasingly adopted for their superior in-reactor performance compared to undoped UO_2, but their spent fuel behaviour, particularly potential Cr speciation and fission product reactivity, remains poorly understood. This investigation has used high energy resolution fluorescence detected X-ray absorption near edge structure (HERFD-XANES) spectroscopy to examine speciation of Cr and Pr/Gd within 200 ppm Cr-doped $(U^{4.4+}_{0.7}Pr^{3+}_{0.3})O_{2-x}$ and 200 ppm Cr-doped $(U^{4.4+}_{0.7}Gd^{3+}_{0.3})O_{2-x}$ compounds. Despite both being UO_2 soluble and undersaturated, analysis indicates that Cr^{3+} and Pr^{3+}/Gd^{3+} form perovskite type $(Pr^{3+}/Gd^{3+})Cr^{3+}O_3$ phases, consistent with classical "grey phases" of spent fuel. The radiation tolerance of these phases was examined via swift heavy ion irradiations of $PrCrO_3$ and $GdCrO_3$ compounds where electron microscopy and grazing incidence synchrotron diffraction indicate significant amorphization but retention of the crystal structure. The investigation highlights the pertinence of considering the chemistry of dopants used for nuclear fuel enhancements regarding their speciation during irradiation and subsequent occurrence within spent fuel.

Amid the accelerating global shift towards carbon neutrality and uncertainties in energy security, nuclear energy is demonstrating its potential by offering safe, reliable base-load power and sovereign control. Concurrently, there remain unavoidable challenges related to the management of spent nuclear fuel (SNF). While some countries, such as France and Russia, favour SNF reprocessing[1,2], currently others, such as Germany, Sweden, Finland and the US, are leaning towards direct disposal[2,3]. Invariably, reducing SNF volumes is a desirable goal from both economic and security perspectives. This creates a demand for fuel types that maximise energy output while minimising SNF production. In this regard, the utilisation of advanced technology nuclear fuels (ATFs) emerges as a promising prospect, holding significant potential in this context. This is exemplified by uranium dioxide (UO_2) nuclear fuel doped with chromium (Cr), which has garnered considerable interest from industry and academia due to its significant grain growth properties[4–6]. Cr-doped UO_2 fuel with larger grains exhibits improved fission gas retention[7], allowing longer irradiation in the reactor without compromising fuel stability, and thus enabling higher burn-ups, consequently reducing SNF generation. Additionally, such fuel provides improved pellet-cladding interaction margins[8–10]. Overall, Cr-doped UO_2 ATFs provide superior performance over undoped UO_2 nuclear fuel. However, the behaviour and precise characteristics of ATFs as SNF are not well defined due to their recent introduction to nuclear power reactors.

Doping UO_2 with relatively low concentrations of Cr at the ppm level results in a relatively significant increase in grain size, ranging from 60 to 70 μm for 500 ppm of Cr to 80–90 μm for 1700 ppm[4,5]. Subsequently, the typical amount added in industry production is targeted at approximately 700–1100 ppm Cr[11,12] to minimise the impact of it as a neutron poison whilst maximising grain growth. The mechanism of grain growth is understood to arise by thermodynamic processes occurring during sintering, either due to the formation of a eutectic phase by Cr, or due to the direct Cr incorporation into the UO_2 lattice with subsequent defect introduction, which both encourage ion transport and grain coalescence during sintering[5,13,14]. Sintering process parameters such as the oxygen partial pressure (μ_{O2}) and temperature (T) directly affect the solubility of Cr in the UO_2 matrix, in which metallic and oxide Cr secondary phases occur as precipitates and along grain boundaries[5,15–19]. In the case of $T = 1700$ °C and $\mu_{O2} = -420$ kJ/mol, the Cr solubility limit is understood to be approximately 500 ppm Cr[5,19]. However, this chemical description only applies to fresh Cr-doped

[1]Institut of Fusion Energy and Nuclear Waste Management (IFN-2), Forschungszentrum Jülich GmbH, Jülich, Germany. [2]Institute of Resource Ecology, Helmholtz Zentrum Dresden-Rossendorf, Dresden, Germany. [3]The Rossendorf Beamline at ESRF, The European Synchrotron, Grenoble, Cedex, France. [4]Department and Chemical and Bioengineering, Princeton University, Princeton, NJ, USA. [5]Institut für Geowissenschaften, Goethe-Universität Frankfurt, Frankfurt am Main, Germany. [6]ESRF, 71 avenue des Martyrs, Grenoble, France. ✉e-mail: d.shirokiy@fz-juelich.de; g.murphy@fz-juelich.de

UO_2 fuel. During irradiation in the reactor and subsequent processing stages, changes in the oxygen potential occur due to fuel burn-up arising primarily from the formation and decay of fission products (FPs). These changes can affect the chemical speciation of Cr, and there is limited existing data on this arising from associated SNF specimens due to their recent deployment in power reactor units. Understanding this speciation is important as it can affect the stability of SNF during interim storage and final disposal.

In the absence of sufficient direct SNF data, model systems enable the investigation of individual effects without the radiation risks and material complexity inherent in real SNF[20]. The production of accurate and representative model system materials, in combination with high-resolution measurement techniques, such as synchrotron X-ray diffraction (S-XRD) and high-energy resolution fluorescence-detected X-ray absorption near-edge structure (HERFD-XANES), can enable the precise determination of the material chemistry within doped spent UO_2 fuel materials[18,21–23]. A particular facet of such fuel that has received little attention is the potential interaction of Cr with fission products, particularly lanthanides (*Ln*) and with transmutation products, such as minor actinides (*MA*) and plutonium (Pu), that alike with Cr, are soluble within the UO_2 lattice matrix and are all expected to gain significant yield in higher burn-up fuels. Cardinaels et al.[24], examined the simultaneous presence of Cr and Gd in UO_2 via microscopy methods, finding that these elements compete with each other in the solid solution, and thus, as the Gd content increases, the solubility limit of Cr decreases, driving it to precipitate at the grain boundaries. In contrast, a favourable interaction between Pu^{3+} and Cr, resulting in the formation of a $PuCrO_3$ perovskite type phases, has been suggested by both computational calculations[25] and the experimental observations via Cr and Pu oxide investigations[26]. It is then postulated that, given the similarity of the ionic radii[27] of trivalent *MA*'s and *Ln*'s to that of Pu, similar perovskite phases based on Cr can also be formed with these elements within UO_2 fuel. Moreover, it was suggested that certain *Ln*'s tend to migrate from the UO_2 matrix towards grain boundaries[28], where the concentration of Cr is higher, thus further inducing a reaction between these elements. Mieszczynski et al.[29], using Cr K-edge microbeam X-ray absorption spectroscopy (XAS) spectra for fresh and spent Cr-doped UO_2 found no significant alterations to the chemistry of Cr between the fresh and spent states. Notably, this study employed standard X-ray absorption spectroscopy analysis on the Cr K-edge, in which the spectral broadening can readily reduce the ability to identify changes to Cr chemical states that may occur during fuel irradiation. The pertinence of deploying HERFD-XANES measurements for fresh Cr-doped UO_2 has recently demonstrated its ability to precisely identify and discern specific Cr phases present in the investigated materials[18]. However, so far, such measurements have not yet been performed on UO_2 materials simultaneously doped with both Cr and *Ln*/*MA*/Pu relevant to SNF. Consequently, it is important to establish precisely how Cr speciates when encountering these UO_2 lattice matrix soluble elements within Cr-doped spent UO_2 fuel, via high-resolution methods, in order to support the safe disposal of SNF.

To shed further light on potential Cr speciation within Cr-doped UO_2 SNF, this investigation has used HERFD-XANES spectroscopy to determine changes in the chemical state of Cr within 200 ppm Cr-doped $(U_{0.7}Ln_{0.3})O_{2-x}$ materials using praseodymium (Pr) which can act as a structural surrogate for Pu^{3+}[27], and gadolinium (Gd), a known neutron absorber, that is introduced in fuels, including ATFs, often to allow for more stable power ramping during reactor startup[30]. Although Ce is a well-known surrogate for Pu when both considered tetravalent, the sensitive redox chemistry of Ce makes it difficult to control when wanting to examine the chemistry of trivalent Pu. When Pu is trivalent, it possesses an ionic radii of 1.00 Å, compared to Pr^{+3}, which has a radii of 0.99 Å. Accordingly, Pr^{3+} is considered a good surrogate cation for examining potential Pu^{3+} reactivity. The subsequent analysis identifies the occurrence of mixed Cr and *Ln* phases consistent with perovskite-type formulation of the general formula $LnCrO_3$ arising from the interaction between Cr and *Ln*'s within the bulk material. To probe the possible stability of these phases within Cr-doped UO_2 SNF, their radiation damage tolerance was examined via swift heavy ion irradiation using 1.3 GeV $^{197}Au^{+}$ ions with a flux of 2×10^9 ions $\times$ cm^{-2} s^{-1} and analysed with scanning electron microscopy (SEM) and synchrotron X-ray grazing incidence diffraction (GIXRD). The results of this investigation are discussed in relation to Cr speciation in Cr-doped UO_2, the formation of novel Cr-based fission product secondary phases not found in undoped UO_2-based SNF, which can affect the stability of this type of fuel during interim and final disposal.

Methods

Materials and synthesis

Undoped UO_2, Cr-doped UO_{2-x} and Cr-doped $(Pr/Gd, U)O_{2-x}$ pellets were synthesised using an established co-precipitation method followed by high temperature sintering[31]. Nitrates of the metals: $UO_2(NO_3)_2{\cdot}6H_2O$, $Cr(NO_3)_3{\cdot}9H_2O$ (Merck KGaA, 98.0%), $(Pr/Gd)(NO_3)_3{\cdot}6H_2O$, (ThermoFisher GmbH, 99.9%) were mixed for doped compounds to achieve the desired composition: 200 ppm of Cr addition for each composition, and 30% molar of each of *Ln* (see Table 1). The solutions were then precipitated with ammonia (25%), that was in 300% excess, centrifuged and washed with deionised water. The Cr content was selected to stay below the Cr solubility limit of 500 ppm at the selected sintering parameters[5,19], with the objective to probe speciation effects within the UO_2 lattice matrix between *Ln* and Cr, while minimising inadvertent reactivity from secondary phases. The resulting material was calcinated at 800 °C for 8 h in air, followed by a reduction step carried out in a tube furnace (ENTECH ESTF 50-18-SP-VK, Ängelholm, Sweden), that was heated to 600 °C for 5 h and cooled to room temperature at a rate of 6 °C/min in controlled 4% H_2 + 96% Ar atmosphere to transform U_3O_8 into UO_2 powder. This powder was then pressed into pellets, each weighing ~1 g, using a tungsten carbide piston in a uniaxial press (Hahn & Kolb, MP12, Stuttgart, Germany), applying a pressure of 574 MPa, followed by a sintering step. Sintering was carried out at $T = 1700$ °C for 10 h under $\mu_{O2} = -420$ kJ/mol conditions, achieved by precise flow rate control of a gaseous mixture of 4%H_2 + 96%Ar and 1% O_2 + 99%Ar. The furnace was cooled to room temperature at a rate of 6 °C/min while the gas atmosphere was kept consistent. Post-sintering, the samples were examined via X-ray diffraction (XRD) analysis collected on powdered specimens using a Bruker D4 diffractometer, which indicated the formation of single-phase fluorite-structured compounds consistent with the UO_2 structure (see Supplementary Note 1).

$PrCrO_3$ and $GdCrO_3$ perovskite pellets were synthesised using a similar approach to that used for UO_2 materials, using a co-precipitation followed by a high-temperature sintering method. $Cr(NO_3)_3{\cdot}9H_2O$ (Merck KGaA, 98.0%), $Pr(NO_3)_3{\cdot}6H_2O$ and $Gd(NO_3)_3{\cdot}6H_2O$ (ThermoFisher GmbH, 99.9%) nitrates were mixed at a 1:1 ratio for desired compositions, precipitated with 25% ammonia solution (300% excess). After washing of the solutions, the samples were dried overnight at 120 °C. The resulting solids were ground into a powder using a mortar and pestle, then calcined at 600 °C for 3 h and at a rate of 6 °C/min cooled to room temperature. For each sample, pellets of ~1 g were then pressed with a tungsten carbide piston in a uniaxial press, with an applied pressure of 574 MPa, and sintered at 1600 °C for 5 h in the reducing 4% H_2 + 96% Ar atmosphere, which, after cooling to room temperature at a rate of 6 °C/min produced pellets which both possessed a green colour. The density of these was determined using hydrostatic weighing with values of 6.601 g/cm^3 (95% of theoretical) for $PrCrO_3$ and 7.045 g/cm^3 (92% of theoretical) for $GdCrO_3$ found. After SEM imaging, the synthesised pellets were polished to prepare it for ion irradiation. The ceramic samples were examined using XRD to confirm product formation and subsequently used for further measurement and analysis (see Supplementary Note 1).

Synchrotron X-ray diffraction

S-XRD measurements were performed at BM20 Rossendorf Beamline (ROBL)[32] of the European Synchrotron Radiation Facility (ESRF) in Grenoble, France on undoped UO_2, Cr-doped UO_{2-x} and 200 ppm Cr-doped $(U_{0.7}Pr_{0.3})O_{2-x}$ and $(U_{0.7}Gd_{0.3})O_{2-x}$ samples. Diffraction data were collected

Table 1 | Refined lattice parameters and goodness-of-fit values determined using the Rietveld refinement against the collected S-XRD diffractograms at the ambient temperature with λ = 0.7377 Å

Sample composition	Lattice parameter, a, Å	Rwp / Rp factors
UO_2	5.470005(5)	10.26% / 7.31%
200 ppm Cr-doped UO_{2-x}	5.469651(2)	8.57% / 6.16%
200 ppm Cr-doped $(U_{0.7}Pr_{0.3})O_{2-x}$	5.463822(2)	8.40% / 6.39%
200 ppm Cr-doped $(U_{0.7}Gd_{0.3})O_{2-x}$	5.418034(4)	12.49% / 8.26%

using the high-resolution XRD diffractometer of BM20, that was equipped with a Dectris Eiger cadmium telluride (CdTe) 500K photon counting detector at a temperature of 23 °C. Prior to measurement, the samples were ground into a fine powder and loaded into 0.3 mm diameter glass and further confined within Kapton tubes for safety. The monochromator energy was calibrated against the K-edge X-ray absorption spectrum of an yttrium metal foil using the first inflection point at 17,038 eV, which provides an uncertainty of ±0.3 eV (±0.000013 Å). Experiments were conducted in transmission mode, and the resulting two-dimensional data were reduced using the PyFAI library, which had been adapted for diffractometers mounted on a goniometer arm[33]. The detector setup was calibrated by measuring a LaB_6 NIST reference standard, and a wavelength of 0.7377 Å determined. The data was collected in the 2θ range of 0–60°, at which diffractograms were analysed using the Rietveld method as implemented in the programme with GSAS-II[34]. The scale factor, background, instrument parameters (including zero point) and the lattice parameters were together refined in relevant structural models.

High energy resolution fluorescence detected X-ray absorption near-edge structure spectroscopy

U M_4-edge and Cr K-edge HERFD-XANES measurements were performed at BM20 ROBL[32] of the ESRF in Grenoble, France. The incident energy was scanned using a Si(111) monochromator around the corresponding edges. Two Si mirrors before and after the monochromator were used to collimate the beam, reject higher harmonics and focus on the sample. The beam size was estimated to be 30 µm vertically and 1000 µm horizontally. The spectra were collected at ambient temperature using an X-ray emission spectrometer[35] equipped with five crystal analysers (Si(220) at 75° Bragg angle for U and Ge(422) at 82.5° Bragg angle for Cr) with 1 m bending radius, and a silicon drift X-ray detector in a vertical Rowland geometry. The spectrometer was tuned to the maximum intensity of the emission line of the corresponding element ($K\alpha$ = 5414.9 eV for Cr and $M\beta$ = 3339.8 eV for U) in non-resonant mode (at incident energy above the corresponding edge). The calibration of the incident monochromatic energy was performed by assigning the maximum of the HERFD-XANES spectrum of reference compounds: that of UO_2 to 3725 eV, and that of Cr(met) to 6006.5 eV. All measurements were performed at 25 °C.

The quantitative amounts of U^{4+} and U^{5+} in the investigated samples were calculated on the U M_4-edge using iterative transformation factor analysis (ITFA)[36,37]. The collected Cr K-edge spectra were analysed to determine the 'best fit' linear phase composition. This was achieved by solving a nonlinear constrained optimisation problem using the Sequential Least Squares Programming (SLSQP)[38] algorithm, which is also employed for various other problems when analysing XAS data[39–41]. To match the energy values, the collected Cr K-edge spectra were linearly interpolated, after which the SLSQP algorithm was used to find:

$$\min_{\bar{w}} \sum_{i=1}^{N} \left(I_{sample}(E_i) - \sum_{j=1}^{n} w_j \cdot I_j(E_i)\right)^2 \quad (1)$$

with N – number of energy points at which the sample was measured, $I_j(E_i)$ – the intensity from phase j at energy E_i, w_j – the weight of phase j, n – number of phases, and the restraints are: $w_j \geq 0$ and $\sum_{j=1}^{n} w_j = 1$.

Swift heavy ion irradiation

The polished surfaces of the perovskite samples were irradiated by the Universal Linear Accelerator (UNILAC) at the GSI Helmholtz Centre for Heavy Ion Research in Darmstadt, Germany. To simulate the harsh reactor conditions, the samples were exposed to a beam of $^{197}Au^{+}$ ions with initial kinetic energy of 1.7 GeV, which by the moment of impact had been reduced to 1.3 GeV by energy reduction in-beam flux detector of 3 µm aluminium (Al) and the 13 µm Al foil used for sample wrapping. The beam flux of 2×10^9 ions × cm^{-2} s^{-1} resulted in an accumulated fluence of 2×10^{12} ions × cm^{-2} (estimated uncertainty ~10%). No active cooling was employed during the sample irradiation process. The depth of radiation damage was estimated using 'The Stopping and Range of Ions in Matter' (SRIM)[42] modelling program with parameters matching those of the experiment. The results are presented in Supplementary Note 2. Pursuant to the irradiation process, the samples were then subjected to a period of repose, the duration of which was sufficient to permit the activation products to decay to levels that are below the detection limit. Prior to the subsequent analysis by GIXRD, the irradiated surfaces were re-examined by SEM.

Scanning electron microscopy

The morphology of radiation-damaged perovskite materials was examined using an Apreo 2 C LoVac scanning electron microscope (ThermoFisher, The Netherlands). The unpolished, pristine and polished irradiated surfaces of the samples were measured. Secondary electron (SE) images were collected due to the charging effect either at 5 or at 2 kV at a working distance of 10 mm.

Grazing incidence X-ray diffraction

Analysis of the structure of irradiated surfaces of perovskite samples using GIXRD was performed on beamline ID22[43] at ESRF, Grenoble, France. The data were collected using a highly collimated, monochromatic beam coupled with a 13-channel silicon 111 multi-analyser stage positioned between the sample and a Dectris Eiger2 X 2M-W cadmium telluride (CdTe) pixel detector. The initial X-ray energy of 11.5 keV was refined following calibration using a LaB_6 pellet standard reference with a precise wavelength of 1.0785 Å determined. To calculate the penetration depth of X-rays, the Glancing Incidence X-ray Analysis (GIXA) utility was used, based on data from Henke et al.[44]. The penetration depth is the distance travelled by the X-ray beam before its intensity is reduced to 1/e. Accordingly, three penetration depths cover approximately 95% of the X-ray beam attenuation. Thus, the grazing angles were selected based on the depth of radiation damage by ions that had been determined (see above) and the calculated depth of X-ray penetration[44] (see Supplementary Note 3) as follows: 1°, 5°, 10°, and 14°. Pristine pellets that were not irradiated were measured at an angle of 14° for comparison.

Results

Synchrotron X-ray diffraction

XRD measurements revealed that the synthesised 200 ppm Cr-doped $(U_{0.7}Pr_{0.3})O_{2-x}$ and $(U_{0.7}Gd_{0.3})O_{2-x}$ pellets adopted a single-phases consistent with UO_2 fluorite structure; the Rietveld profiles are provided in Supplementary Note 1. However, lab XRD is known to be relatively insensitive to the effects of trace doping[22]. Therefore, in order to examine trace phase separation and determine the high-resolution structures of the examined materials, high-resolution S-XRD measurements were performed. The diffractograms with Rietveld refinement profiles are provided in Fig. 1 and the determined values are provided in Table 1.

A Rietveld analysis of the collected S-XRD diffractograms indicated that, within the limits of resolution, all materials are single-phase in fluorite-structure space group $Fm\bar{3}m$ consistent with UO_2. In the case of the 200

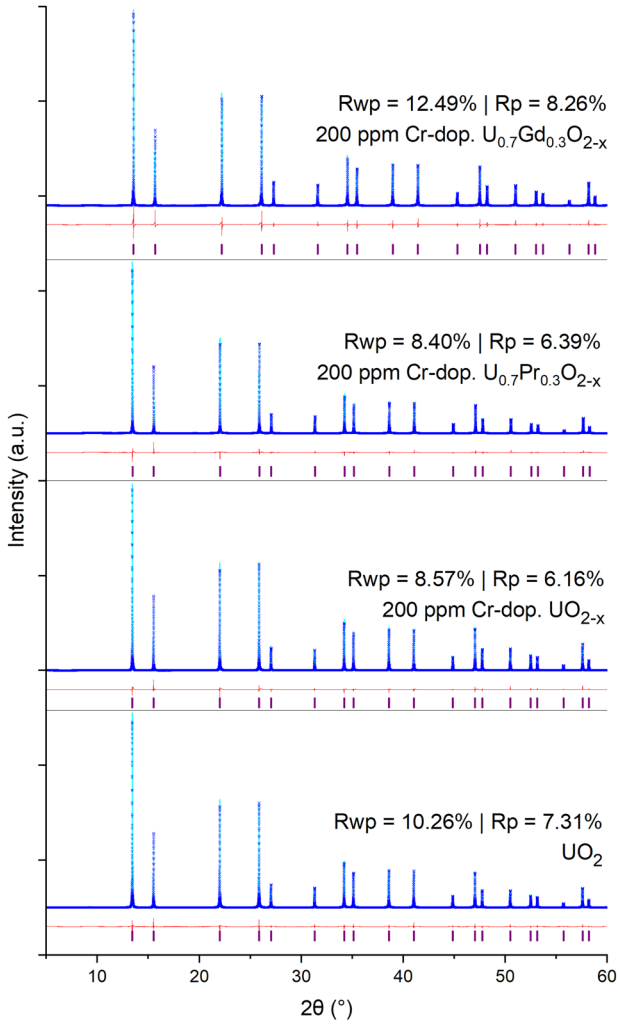

Fig. 1 | Rietveld refinement of S-XRD measurements of pure UO_2, 200 ppm Cr-doped UO_{2-x} and 200 ppm Cr-doped $(U_{0.7}Pr_{0.3})O_{2-x}$ and $(U_{0.7}Gd_{0.3})O_{2-x}$ samples. It is notable that in the presence of dopants, peak shifting to a higher angle is observed, corresponding to a decrease in the lattice parameter. Measured data, refined models, difference curve and allowed reflections of the $Fm\bar{3}m$ space group for fluorite UO_2 are respectively represented by blue markers, cyan lines, red lines and purple vertical markers.

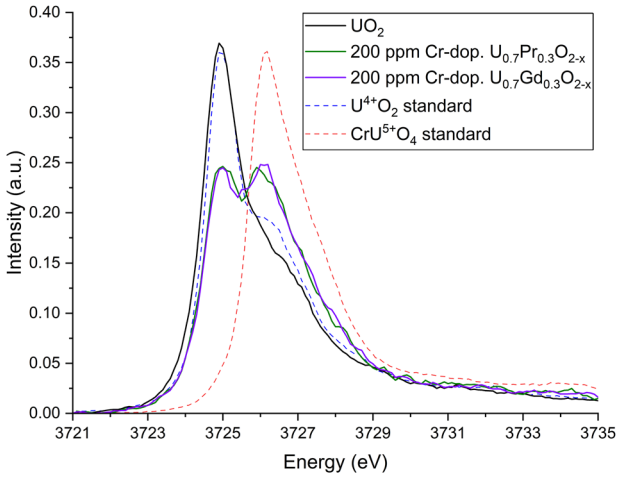

Fig. 2 | Normalised HERFD-XANES U M_4-edge spectra as solid lines for pure UO_2, and 200 ppm Cr-doped $(U_{0.7}Pr_{0.3})O_{2-x}$ and $(U_{0.7}Gd_{0.3})O_{2-x}$. The dashed lines indicate reference spectra for collected standards as $U^{4+}O_2$ and $CrU^{5+}O_2$. The spectra of the doped samples, which exhibit an additional peak, demonstrate that the presence of 30% trivalent *Ln*'s causes the oxidation of U^{4+} to U^{5+}. The measured UO_2 sample was found to be closer to U^{4+} than the standard spectra, due to slight oxidation of the UO_2 reference.

ppm Cr-doped UO_{2-x} sample, a contracted lattice parameter is observed. This indicates incorporation of Cr^{3+} in the UO_2 lattice by creating oxygen vacancies[22]. Invariably, secondary phase occurrence pertaining to Cr-O and Cr metallic phases can readily occur due to the diffusion kinetics and thermodynamic distribution of Cr during sintering[18]. Nevertheless, such phases are not readily observed in S-XRD measurements. Trivalent *Ln*'s are well understood to form a solid solution with U in doped UO_2 through a charge compensation mechanism up to 50%[45], which for prescribed molar amounts of Pr^{3+} and Gd^{3+} is achieved through the oxidation of U^{4+} to U^{5+} and lattice contraction, the extent of which depends on the type and amount of *Ln* incorporated[46–50]. This trend can be readily observed in the results of Table 1.

High energy resolution fluorescence detected X-ray absorption near-edge structure spectroscopy analysis

Although S-XRD analysis has demonstrated that all investigated UO2-based samples appear to be single-phase, the trace amount of Cr doping, coupled with the ability of Cr to adopt different chemical states within the bulk UO_2, has previously been shown to be difficult to track using diffraction methods[18]. XANES is an excellent tool for determining the chemistry of dopants, with particular efficacy in determining their oxidation state when present at trace amounts, which has been demonstrated well in the context of doped UO_2 materials[18,23,29,51]. However, challenges persist, particularly for the Cr K-edge and U M_4-edge in standard XANES measurements due to core-hole lifetime broadening. Consequently, to overcome this, HERFD-XANES measurements were performed at the Cr K-edge and, to confirm the bulk behaviour of UO_2, at the U M_4-edge.

Figure 2 shows the normalised U M_4-edge HERFD-XANES spectra for the UO_2 and 200 ppm Cr-doped $(U_{0.7}Pr_{0.3})O_{2-x}$ and $(U_{0.7}Gd_{0.3})O_{2-x}$ samples with a $U^{4+}O_2$ and $CrU^{5+}O_4$ standard. In the case of the UO_2 sample, the sample is purely tetravalent to the limits of resolution. In contrast, the 200 ppm Cr-doped $(U_{0.7}Pr_{0.3})O_{2-x}$ and $(U_{0.7}Gd_{0.3})O_{2-x}$ samples show oxidation consistent with U^{5+} but also retention of U^{4+}. This oxidation state is indicative of aliovalent oxidation of U due to the inclusion of Pr^{3+} and Gd^{3+} within the UO_2 structure[46,47]. Using ITFA for calculating the quantitative amounts of U oxidation states in the measured samples it was determined that the U^{4+}/ U^{5+} ratio is 0.66/0.34 in the 200 ppm Cr-doped $(U_{0.7}Pr_{0.3})O_{2-x}$ sample and 0.64/0.36 in the 200 ppm Cr-doped $(U_{0.7}Gd_{0.3})O_{2-x}$ sample. Given the known 5% ITFA calculation error[36], the calculations show that the incorporation of Pr^{3+} and Gd^{3+} leads to the expected oxidation of U consistent with literature[52,53]. The compounds are accordingly written as 200 ppm Cr-doped $(U^{4.4+}_{0.7}Pr^{3+}_{0.3})O_{2-x}$ and 200 ppm Cr-doped $(U^{4.4+}_{0.7}Gd^{3+}_{0.3})O_{2-x}$.

HERFD-XANES data at the Cr K-edge obtained on 200 ppm Cr-doped $(U_{0.7}Pr_{0.3})O_{2-x}$ and $(U_{0.7}Gd_{0.3})O_{2-x}$ samples were compared with those from perovskite $PrCrO_3$ and $GdCrO_3$ samples, as well as with previously analysed Cr standards[18]: metallic Cr^0, $Cr^{+2}Cl_2$, $Cr^{+3}Cl_3{\cdot}6H_2O$, and $Cr^{+3}{}_2O_3$. The spectra were also compared with the previously measured Cr K-edge of a *Ln*-free UO_2 sample doped with Cr at 2395 ppm[18], synthesised using the identical synthesis conditions, and a Cr^{3+}-doped UO_2 single crystal extracted from the same sample[18], in order to further examine differences in Cr chemistry in UO_2 with and without *Ln* present. The normalised HERFD-XANES Cr K-edge spectra for these combined measurements is provided in Supplementary Note 4. Clear from this plot is the 200 ppm Cr-doped $(U_{0.7}Pr_{0.3})O_{2-x}$ and $(U_{0.7}Gd_{0.3})O_{2-x}$ samples match closely with Cr^{3+} standards. Accordingly, for simplicity Fig. 3 plots the normalised Cr K-edge HERFD-XANES results for the 200 ppm Cr-doped $(U_{0.7}Pr_{0.3})O_{2-x}$ and $(U_{0.7}Gd_{0.3})O_{2-x}$, with just the Cr^{3+} standards including $PrCr^{+3}O_3$ and

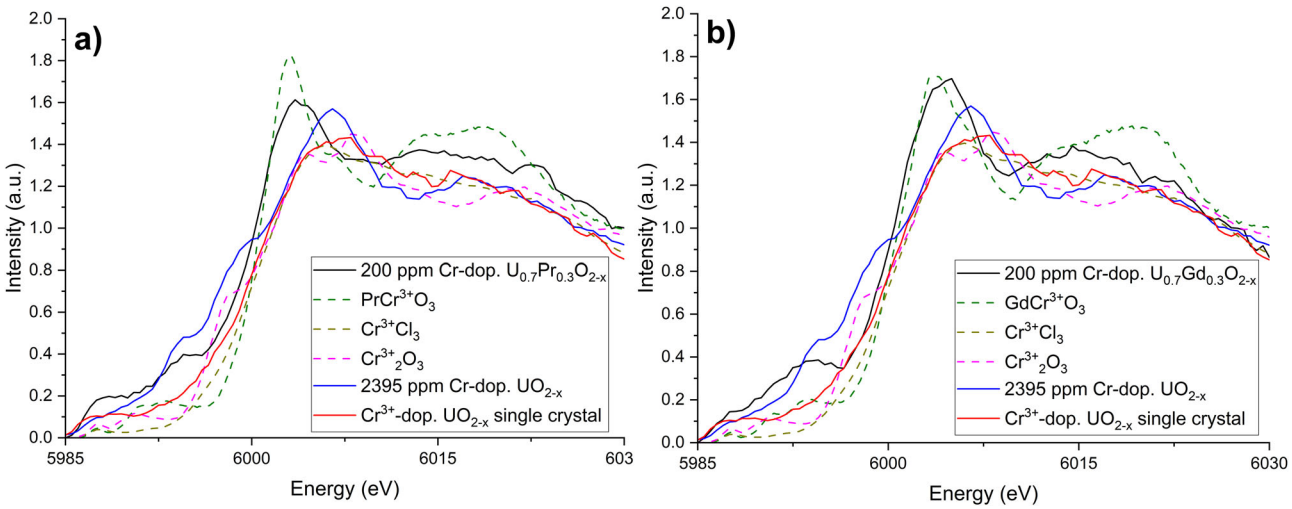

Fig. 3 | Normalised HERFD-XANES Cr K-edge spectra. Cr-doped **a** $(U_{0.7}Pr_{0.3})O_{2-x}$ and **b** $(U_{0.7}Gd_{0.3})O_{2-x}$ samples compared with the Cr^{3+} standards (dashed lines): $LnCr^{3+}O_3$, $Cr^{3+}Cl_3$[18], $Cr^{3+}{}_2O_3$[18], as well as the *Ln*-free, 2395 ppm Cr-doped UO_2 bulk sample[18] and Cr^{3+}-doped UO_2 single crystal[18]. The position and shape of the main peak indicate a pronounced similarity between the sample and the $GdCrO_3$ material, whilst highlighting its difference from the other 3+ standards and *Ln*-free samples.

Table 2 | The SLSQP results of calculating the linear phase composition for the normalised HERFD-XANES Cr K-edge spectra of 200 ppm Cr-doped $(U_{0.7}Pr_{0.3})O_{2-x}$ and $(U_{0.7}Gd_{0.3})O_{2-x}$ samples

Sample	Phase	Weight
	Cr^0	22%
	$Cr^{2+}Cl_2$	2%
200 ppm Cr-doped $(U_{0.7}Pr_{0.3})O_{2-x}$	$PrCr^{3+}O_3$	68%
	$Cr^{3+}Cl_3$	0%
	$Cr^{3+}{}_2O_3$	8%
	Cr^0	20%
	$Cr^{2+}Cl_2$	3%
200 ppm Cr-doped $(U_{0.7}Gd_{0.3})O_{2-x}$	$GdCr^{3+}O_3$	75%
	$Cr^{3+}Cl_3$	2%
	$Cr^{3+}{}_2O_3$	0%

$GdCr^{+3}O_3$, 2395 ppm Cr-doped UO_2 sample[18], and a Cr^{3+}-doped UO_2 single crystal extracted from the same material body[18].

The Cr-doped UO_2 single crystal extracted from the bulk Cr-doped UO_2 sample with 2395 ppm addition of Cr, is representative for the Cr^{3+} state in the UO_2 lattice, free from secondary phases that can be observed in the bulk sample in Fig. 3, arising from non-lattice associated Cr^0 (metallic), $Cr^{2+}O$, $Cr^{3+}{}_2O_3$, and other associated secondary phases. As demonstrated in Fig. 3, both the 200 ppm Cr-doped $(U_{0.7}Pr_{0.3})O_{2-x}$ and $(U_{0.7}Gd_{0.3})O_{2-x}$ samples show a considerably different line shape compared to the 2395 ppm Cr-doped UO_2 bulk sample and Cr^{3+}-doped UO_2 single crystal references. This observation is notable given that the synthesis of the 200 ppm Cr-doped $(U_{0.7}Pr_{0.3})O_{2-x}$ and $(U_{0.7}Gd_{0.3})O_{2-x}$ samples was conducted under conditions that are below the solubility limit of Cr in UO_2[19]. Under such conditions, the lattice of UO_2 is undersaturated with Cr, meaning that there is relatively minimal secondary Cr phases available in the bulk. Interestingly, the 200 ppm Cr-doped $(U_{0.7}Pr_{0.3})O_{2-x}$ and $(U_{0.7}Gd_{0.3})O_{2-x}$ sample lines' shape shows signatures that are not consistent with either the single crystal, particularly at the pre-edge, nor the post-edge. Rather, the HERFD-XANES spectra of the 200 ppm Cr-doped $(U_{0.7}Pr_{0.3})O_{2-x}$ and $(U_{0.7}Gd_{0.3})O_{2-x}$ samples show more consistency with that of the corresponding $LnCr^{+3}O_3$ perovskite standards. This result indicates that, compared to the non-doped examples, Cr has undergone speciation away from the UO_2 lattice matrix coupled with like-UO_2 matrix soluble *Ln*'s, towards novel secondary phases of Cr and Pr/Gd mixed-oxide compounds that are consistent with the perovskite structure.

In order to further quantify the changes to the Cr chemical state in the 200 ppm Cr-doped $(U_{0.7}Pr_{0.3})O_{2-x}$ and $(U_{0.7}Gd_{0.3})O_{2-x}$ samples, quantitative analysis using the SLSQP algorithm was performed. The SLSQP algorithm, which employs gradient-based optimisation, solving the minimisation problem (Eq. 1), found the best combination of phase intensities (weighted sum) to match the given sample intensity curve, based on a set of phase spectra. The calculation results are presented as curves in Fig. 4 and as values in Table 2.

As demonstrated in Table 2, the SLSQP analysis results indicate that the predominant proportion of Cr in both the 200 ppm Cr-doped $(U_{0.7}Pr_{0.3})O_{2-x}$ and $(U_{0.7}Gd_{0.3})O_{2-x}$ resides within the perovskite $LnCr^{3+}O_3$ structure, accounting for 68% and 75%, respectively. Minimal amounts of reference $Cr^{3+}Cl_3$ and $Cr^{2+}Cl_2$ are observed, although moderate amounts of Cr^0 are present, which overall is in stark contrast to previous work on Cr-doped UO_2 phase distributions via Cr K-edge HERFD-XANES[18]. This analysis indicates and further supports the previous argument that under the applied sintering conditions in the presence of *Ln*'s, Cr undergoes significant speciation towards secondary non-UO_2 phases. This result appears to validate previous computational works that have examined the formation of similar compounds in Cr-doped UO_2 spent fuels[25].

$PrCr^{3+}O_3$ and $GdCr^{3+}O_3$ are classical ABO_3 perovskites that are orthorhombic in space group *Pbnm*, where the Cr^{3+} cation exhibits a 6-fold coordination environment to O. In contrast, in UO_2, Cr adopts a distorted 6-fold coordination to O, while in $Cr^{3+}{}_2O_3$, it also adopts a distorted 6-fold environment to O. Local environments of Cr within the Cr-doped UO_2, Cr_2O_3 and $LnCrO_3$ structures are shown in Fig. 5. The Cr spectra for the 200 ppm Cr-doped $(U_{0.7}Pr_{.3})O_{2-x}$ and $(U_{0.7}Gd_{.3})O_{2-x}$ samples appear to deviate from the known environments of UO_2 and $Cr^{3+}{}_2O_3$, among others. This deviation is particularly evident in comparison to the fresh Cr-doped UO_2 material, and the spectra indicate a shift towards the $LnCr^{3+}O_3$ perovskite structure. From a thermodynamic perspective, perovskite structures of the formula $LnCr^{3+}O_3$ are characterised by a high degree of stability, which is attributed to a favourable match between the ionic radii of the *Ln* and Cr cations[27]. In comparison, the significant size mismatch between U^{4+} and Cr^{3+} in UO_2 significantly limits the solubility of Cr within UO_2 and accordingly can be considered to be less stable structurally[27]. Pertinently, these results indicate that such phases are

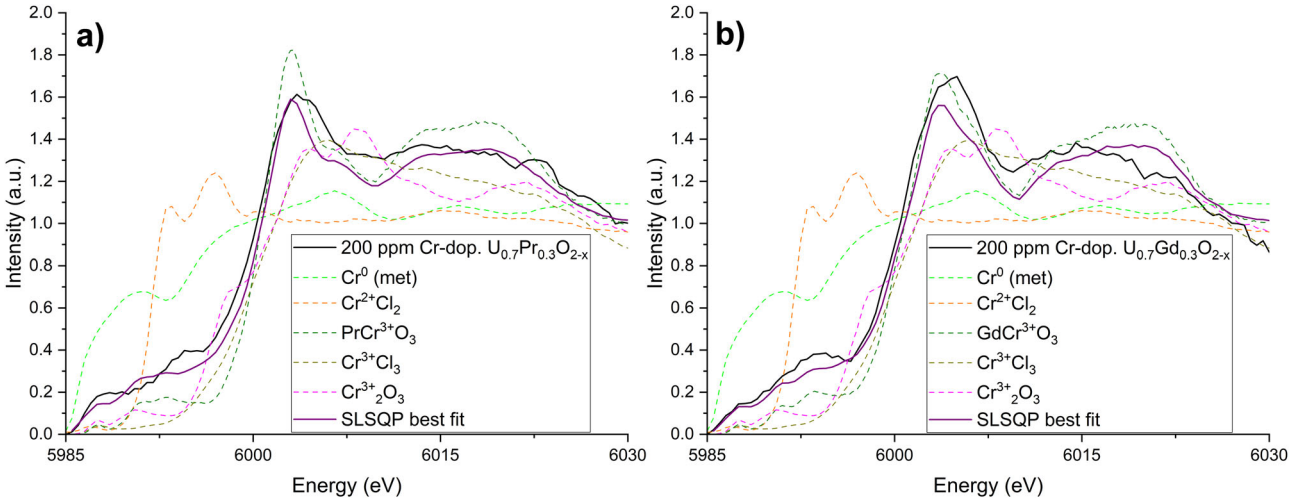

Fig. 4 | The SLSQP results for the normalised HERFD-XANES Cr K-edge spectra of the samples. The best fit for the normalised HERFD-XANES Cr K-edge spectra of 200 ppm Cr-doped **a** $(U_{0.7}Pr_{0.3})O_{2-x}$ (Rwp: 0.0688, χ^2: 0.0057) and **b** $(U_{0.7}Gd_{0.3})O_{2-x}$ (Rwp: 0.0799, χ^2: 0.0078). The spectra of the samples are indicated by a black solid line, the spectra of the phase components are indicated by dotted lines, and the curve of the calculated linear phase composition is indicated by a solid purple line.

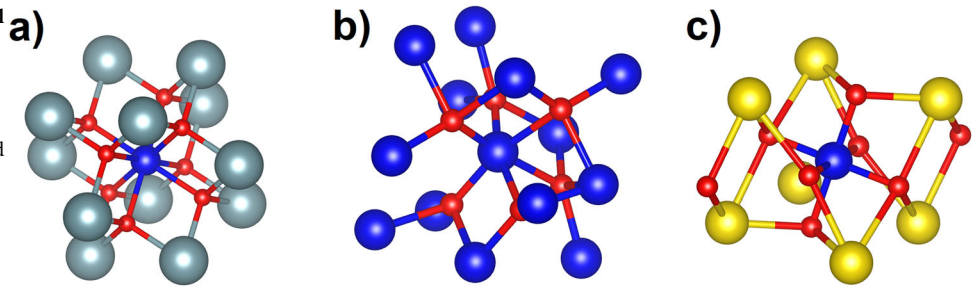

Fig. 5 | Local environment of Cr^{3+} in different local structure configurations. Within **a** Cr^{3+}-doped UO_2[18] in fluorite structured UO_2 in space group $Fm\bar{3}m$ and **b** trigonal $Cr^{3+}{}_2O_3$ in space group $R\bar{3}c$ and **c** $LnCr^{3+}O_3$ in space group $Pbnm$, where Cr atoms shown in blue, U – in grey, *Ln* – in yellow and oxygen in red. Images were generated using open source and access software VESTA[61].

stable host matrices within Cr-doped UO_2-based SNF for both Cr and *Ln* elements to reside.

Radiation damage studies

In considering the HERFD-XANES results, which indicate that speciation occurs in Cr-doped UO_2 in the presence of *Ln*'s towards $LnCrO_3$ mixed oxide structures, it is pertinent to consider the structural and radiation stability of such phases. This is particularly relevant given that they are known to exhibit relatively high thermal and chemical stability[54,55]. In comparison, a lack of knowledge exists pertaining to these particular Cr-based perovskite phases when subjected to radiation damage. Similar studies on related Fe-based perovskites—$LaFeO_3$, under ion irradiation of 2 MeV Kr^+ ions with a fluence of 2×10^{16} ions/cm^2, found that the structure underwent changes in the local environment due to ion irradiation, while retaining their crystalline structure[56]. Subsequently, to shed light on the $LnCrO_3$ radiation damage tolerance when occurring within Cr-doped UO_2 derived SNF, synthesised $PrCrO_3$ and $GdCrO_3$ ceramic pellets were exposed to swift heavy ion irradiation by $^{197}Au^+$ ions with energy of 1.3 GeV and fluence of 2×10^{12} ions $\times$ cm^{-2}. The recovered ion irradiated pellets were found to remain largely intact as standing bodies (Supplementary Note 5). Examination of their microstructure was performed via SEM imaging on both irradiated and pristine samples to contrast microstructural changes. The results are presented in Fig. 6.

The SEM-SE micrographs shown in Fig. 6 reveal the occurrence of apparent melting phenomena on the irradiated surface, which is consistent with the formation of an amorphous glass-like microstructure, attributed to the transformation of an initially sharp crystalline grain structure. In the case of $PrCrO_3$, the grain boundaries on the irradiated surface were largely erased, while the grain boundaries of $GdCrO_3$ were either lost or expanded in width and depth, transforming into pores, potentially due to the initially high porosity of the sample.

To further examine the radiation damage response of the irradiated $PrCrO_3$ and $GdCrO_3$ ceramic samples, particularly probe for potential retention of the crystal structure, synchrotron GIXRD measurements were performed. To verify the precision of the measurements, the anticipated radiation-induced damage depth within the ceramic bodies was determined through SRIM calculations based on the prescribed irradiation conditions. The results, which are provided in Supplementary Note 2, show the stopping range of the ions to be 36.9 µm for $PrCrO_3$ and 34.0 µm for $GdCrO_3$. For GIXRD, an energy of 11.496 eV X-rays, corresponding to a wavelength of 1.0785 Å, was selected, to optimise the measurements. Calculations using GIXA utility[44] and considering the densities of the perovskite samples determined the X-ray penetration depths with a maximum of 3.31 µm for $PrCrO_3$ and 2.44 µm for $GdCrO_3$ at 14° (see Supplementary Note 3), which cover 1/e of the X-ray beam. Consequently, the three penetration depths corresponding to approximately 95% of the X-ray signal being attenuated result in maximum depths of 10 µm, which is below the maximum ion damage depth calculated with SRIM. Subsequently, GIXRD measurements were performed using angles of 1, 5, 10 and 14°, which correspond to 0.23/0.17, 1.18/0.87, 2.37/1.75 and 3.31/2.44 µm for $PrCrO_3$ and $GdCrO_3$ respectively. Inset diffractograms are provided in Fig. 7 in a shortened 2θ range to highlight amorphisation effects respectively whereas complete diffractograms are provided in Supplementary Note 6.

Observing the GIXRD diffractograms of Fig. 7 for $PrCrO_3$ and $GdCrO_3$ indicates that significant amorphisation has occurred, but retention of the crystalline structure is still found. The most significant damage and amorphization is observed at 1°, which corresponds to a stopping range of 230 nm for Pr 169 nm for $GdCrO_3$. In considering the crystalline phases in the

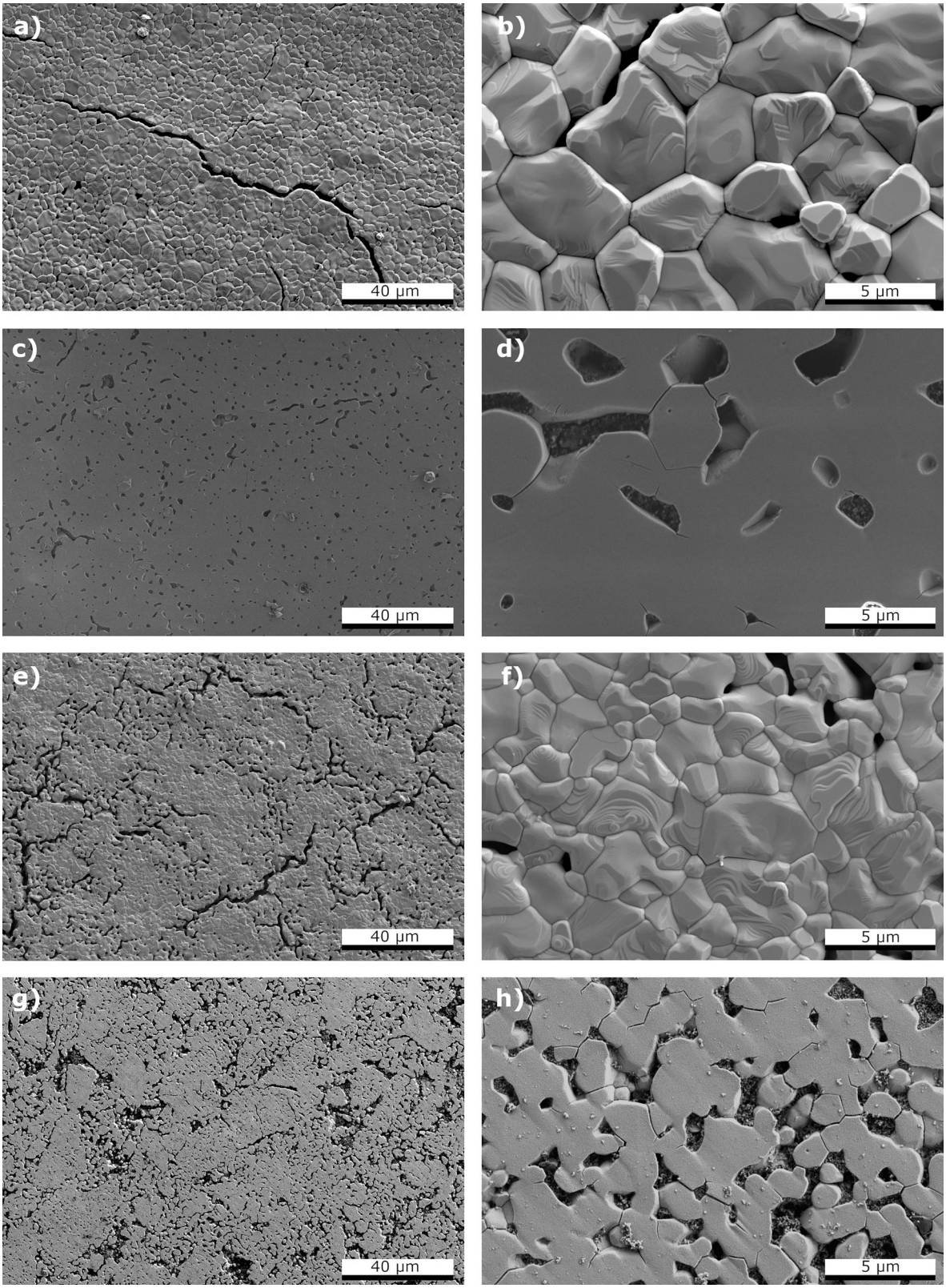

Fig. 6 | SE SEM images of the pristine and irradiated perovskite samples. **a**, **b** $PrCrO_3$ pristine surface, **c**, **d** $PrCrO_3$ after irradiation; **e**, **f** $GdCrO_3$ before and **g**, **h** after irradiation. On the non-irradiated surfaces, grain microstructures can be seen with grain boundaries present. The surfaces after irradiation are observed to exhibit an amorphous microstructure with almost no grain boundaries. Note that prior to irradiation, the surfaces were polished.

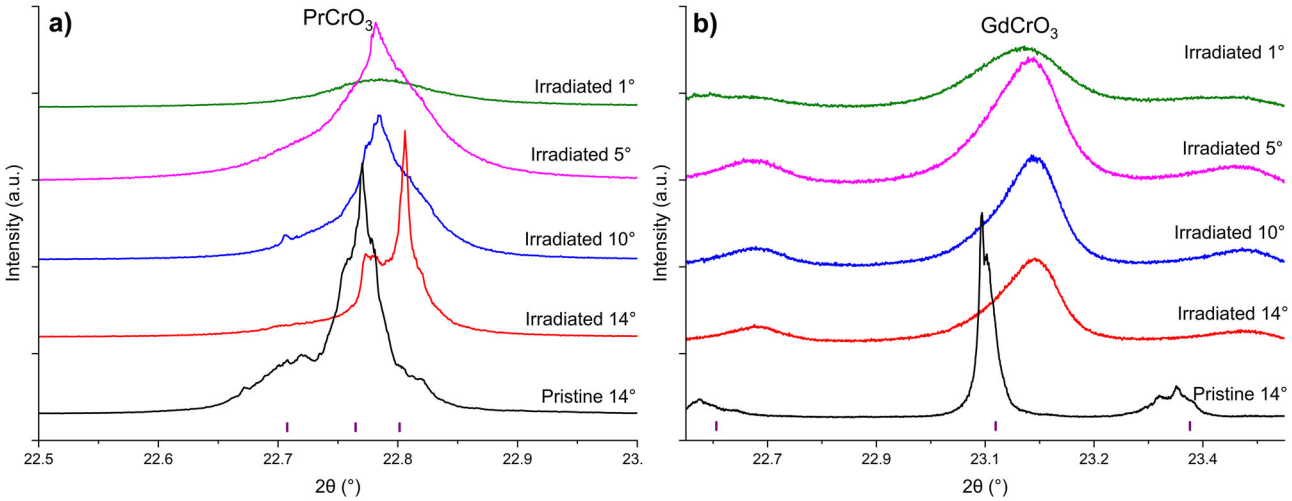

Fig. 7 | Synchrotron GIXRD diffractograms for irradiated perovskite samples. The diffractograms at X-ray wavelength of 1.0785 Å for **a** $PrCrO_3$ in 2θ of 22.5–23.0° and **b** $GdCrO_3$ in 2θ of 22.5–23.4° respectively at variable grazing angles between 1° and 14° and also compared to the non-irradiated pristine surface at grazing angle of 14°. The purple marks represent the positions of the Bragg reflections in orthorhombic *Pbnm* space group of the parent perovskite structures.

samples, it can be observed that Bragg reflections have shifted to higher 2θ, indicating lattice contraction. A comparable preservation of structure was also observed for $LaFeO_3$[56], albeit with lower energies (2 MeV) being used for the irradiation process. Moreover, when one considers the known thermal and chemical stability of *Ln*CrO3-based perovskites[54,55], the radiation damage studies performed indicate occur would ubiquitously within Cr-doped UO_2 SNF.

Discussion

In a traditional undoped UO_2 SNF, the fuel adopts complex main and various secondary phases during irradiation as the fuel matrix takes on a highly complex solid solution due to the occurrence of FPs[57]. The type of phases that are observed in this composite include the UO_2 fuel matrix, bubbles of gaseous FPs and insoluble metallic precipitates, referred to as ε-particles, and oxide compounds known as the "grey phases"[57]. The speciation of particular elements within these phases is determined by their individual chemistries, particularly their reactivity, solubility and redox potentials compared to the UO_2 matrix and the oxygen potential environment of the fuel. In the case of trivalent *Ln*'s and *MA*'s, their similar ionic radii to uranium, the ability for the fluorite lattice to adopt defects through trivalent cation incorporation in addition to the low oxygen potential of the fuel inhibits their formation as separate oxide phases, whilst their redox chemistries compared to UO_2 disfavour metallic formation. Accordingly, these elements are understood and consistently observed to form a complex solid solution with UO_2. In comparison, alkali and alkaline earth metal cations prefer to adopt the "grey phase" components as they're poorly soluble within UO_2 and further their redox chemistry is not favourable. In the "grey phase" formation, they combine typically with higher valent 4 and 5 d transition metal elements such as Zr and Nb, which prefer oxide environments, although can also report to the fuel matrix, and form the 'grey phase' structure, which is typically considered a perovskite formulation chemically, (Cs,Rb,Ba,Sr)(Zr,Nb)O_3[57]. The identified *Ln*CrO_3 type perovskite phases occurs in the studied 200 ppm Cr-doped $(U_{0.7}Pr_{.3})O_{2-x}$ and $(U_{0.7}Gd_{.3})O_{2-x}$ samples via HERFD-XANES analysis, consistent with "grey phase" formulation. However, such phases are not expected to occur in regular non-Cr doped UO_2 fuels, due to the absence of Cr in addition to the general absence of 3 d transition metal elements in the fission product pool[58].

A significant observation made in this investigation is not just the speciation of Cr but also of Pr and Gd, which as described should report to the UO_2 matrix. Indeed, similar model system studies that have used Pr^{3+}, Gd^{3+} and other Ln^{3+} elements under similar synthesis conditions, find single phase solid solution behaviour[59]. Calculating the Goldschmidt tolerance factors for $PrCrO_3$ and $GdCrO_3$ (Eq. 2), which define the stability and relative distortion occurring within a specific perovskite formulation, produces respective values of 0.94 and 0.93 which are relatively stable[27,60]. If hypothetical tolerance factors are calculated for larger 4 and 5 d elements that do exist as fission products with the $Ln^{3+}B^{3+}O_3$ formulation, significantly worse values are obtained that that are not as conducive to stability as the $Ln^{3+}Cr^{3+}O_3$ form. This is due to the size mismatch with the Cr^{3+} coupled with the disfavourable adoption of trivalent oxidation states for most 4 and 5d elements that occur as FPs. Accordingly, the favourable structural chemistry between the Cr^{3+} and Ln^{3+} cations readily facilitates their formation of $Ln^{3+}Cr^{3+}O_3$ within Cr-doped *Ln* bearing UO_2. Critically, given their known high temperature stability coupled with the as-demonstrated reasonable radiation tolerance, suggests that such phases are stable within both irradiated and spent Cr-doped UO_2. Consequently, the results of this investigation suggest Cr, *Ln*'s and potentially *MA*'s, which are otherwise expected to be soluble within the UO_2 matrix, can speciate to form unique, thermally and radiation resistant oxide based "grey phases" within Cr-doped UO_2 SNF.

$$t = \frac{r_A + r_O}{\sqrt{2}(r_B + r_O)} \tag{2}$$

with t—Goldschmidt's tolerance factor, r_A—radius of the cation A, r_B—radius of the cation B, and r_O—ionic radius of oxygen.

Previous investigations examining speciation of Cr within Cr-doped UO_2 actual fresh and irradiated SNF by Mieszczynski et al.[29], using conventional XAS measurements, indicated little change to the Cr state. The lack of observable change can be attributed to the lower resolution measurement as opposed to HERFD-XANES methods, deployed in the present investigation. Beyond SNF studies, Devillaire et al.[17], examined changes to the chemical state of Cr-doped UO_2 by performing gradient temperature effect studies on annular pellets to examine the changes Cr secondary phases, finding fuel relevant oxygen potential has an effect on the chemical state of Cr via electron microprobe analysis. Cardinaels et al.[24], used similar microscopy analysis of model material Gd/Cr-doped UO_2 finding competing chemical effects between Gd and Cr. However, beyond these studies this investigation appears to be the first to use HERFD-XANES to examine and identify the reactivity and formation of distinct Pr/Gd-Cr-O phases within Cr-doped $(Pr^{3+}/Gd^{3+},U)O_{2-x}$ model materials. Considering the similar chemical behaviour with other trivalent *Ln*'s it can be reasonably assumed that reactivity between Cr^{3+} these other *Ln*'s would occur leading

to similar structure formation. Furthermore this can be extended to the behaviour of trivalent actinides such as Pu^{3+} which has been previously calculated to favourably occur within Cr-doped UO_2 SNF as $PuCrO_3$[25]. The similar ionic radii between Pr^{3+} and Pu^{3+} for coordination number of 6, strongly suggests formation of $PuCrO_3$ "grey phases" within Cr-doped UO_2 would be near likely. The 'grey phase' in classical UO2-based SNF has often been observed to occur as precipitates on top of UO_2 grains. However, when one considers recent microscopy evaluations of Cr-doped UO_2, finding significant enrichment along grain boundaries[15], in addition to *Ln*-doped UO_2 thermodynamics investigations which suggest poor mixing of *Ln*'s within UO_2 can lead to enrichment of *Ln*'s in the grain boundary regions[28], this suggests "grey phase" type reactivity can occur equally at both grain boundaries and as precipitates within Cr-doped UO_2 SNF. Such behaviour of particularly *Ln*'s is in contrast to what has been seen in classical UO_2 based SNF and the investigation naturally highlights the pertinence of considering how the chemistry of dopants such as Cr within next generation ATF fuels can influence the chemical state of FP secondary phases and subsequent stability of SNF.

To summarise, it has been demonstrated using HERFD-XANES measurements, that speciation of both Cr and the *Ln*'s: Pr and Gd, occurs within 200 ppm Cr-doped $(U_{0.7}Pr_{.3})O_{2-x}$ and $(U_{0.7}Gd_{.3})O_{2-x}$ sintered materials, forming "grey phase"-like (Pr/Gd)CrO_3 perovskite secondary phases. Their occurrence is attributed to the preferential size match between the Cr^{3+} and Pr^{3+}/Gd^{3+} cations in the oxide state, forming a perovskite formulation that is highly stable when the Goldschmidt tolerance factors for formation are considered. Surprisingly, this reactivity occurs despite the solubility of Cr^{3+} and Pr^{3+}/Gd^{3+} within UO_2 and when present in quantities that should be undersaturated within the matrix. The radiation stability of these phases was examined using swift heavy ions irradiation with ^{197}Au ions. SEM examination of the irradiated surface revealed partial amorphisation of the materials. However, further synchrotron GIXRD measurements of the irradiated materials revealed retention of the crystalline perovskite structure. When the known thermal stability of these phases is considered, the results of this investigation suggest their occurrence within Cr-doped UO_2 based SNF is ubiquitous and considering the related chemistry of *Ln*'s to actinides it implies similar phases would form additionally within these non-UO_2 fuel matrix "grey phases". Considering light transition metal elements like Cr are not expected within regular UO_2 spent fuel, the investigation indicates that the fission product derived phase assemblage within Cr-doped UO_2 ATFs is incongruent in comparison to UO_2 and should be considered in stability and dissolution studies, particularly since such ATF fuels are intended for higher burn up usage and will subsequently possess a greater fission product inventory.

Data availability

The datasets generated and/or analyzed during the current study are not publicly available due to technical limitations related to the scale, variance and non-standardised format of the primary data files, but are available from the corresponding author on reasonable request.

Received: 24 September 2025; Accepted: 27 January 2026;
Published online: 16 February 2026

References

1. NW-T-1.14 (Rev. 1). *Status and Trends in Spent Fuel and Radioactive Waste Management*. (International Atomic Energy Agency, 2022). https://www-pub.iaea.org/MTCD/Publications/PDF/PUB1963_web.pdf.
2. *Management of Spent Fuel from Nuclear Power Reactors*, *IAEA Bulletin*. Vol. 32, (60–2) (International Atomic Energy Agency, 2019). https://www.iaea.org/bulletin/60-2.
3. Spykman, G. Dry storage of spent nuclear fuel and high active waste in Germany-Current situation and technical aspects on inventories integrity for a prolonged storage time. *Nucl. Eng. Technol.* **50**, 313–317 (2018).
4. Bourgeois, L. Effect of additives on enhanced sintering and grain growth in uranium dioxide. Report No. CEA-R-5621, (CEA Centre d'Etudes de Grenoble, 1993).
5. Bourgeois, L., Dehaudt, P., Lemaignan, C. & Hammou, A. Factors governing microstructure development of Cr-doped UO_2 during sintering. *J. Nucl. Mater.* **297**, 313–326 (2001).
6. Delafoy, C., Dewes, P. & Miles, T. Areva NP Cr_2O_3-doped fuel development for BWRs. *American Nuclear Society—2007 LWR Fuel Performance/Top Fuel* (2007).
7. Kashibe, S. & Une, K. Effect of additives (Cr_2O_3, Al_2O_3, SiO_2, MgO) on diffusional release of ^{133}Xe from UO_2 fuels. *J. Nucl. Mater.* **254**, 234–242 (1998).
8. Arborelius, J. et al. Advanced doped UO_2 pellets in LWR applications. *J. Nucl. Sci. Technol.* **43**, 967–976 (2006).
9. Killeen, J. C. Fission gas release and swelling in UO_2 doped with Cr_2O_3. *J. Nucl. Mater*. https://doi.org/10.1016/0022-3115(80)90272-X (1980).
10. Turnbull, J. A. Effect of grain-size on swelling and gas release properties of UO_2 during irradiation. *J. Nucl. Mater.* **50**, 62–68 (1974).
11. Wright, J., Arborelius, J. & Backman, K. Development of Westinghouse advanced doped pellet technology. Report No. HPR-364-V2, 203–217 (Lillehammer, Norway, 2005).
12. Cole, S. E., Delafoy, C., Graebert, R., Louf, P. H. & Teboul, N. AREVA optimized fuel rods for LWRs. (TopFuel, Manchester, UK, 2012).
13. Olshanskii, Y. I. & Shlepov, V. K. Sistema Cr-Cr_2O_3. *DOKLADY AKADEMII NAUK SSSR* **91**, 561–564 (1953).
14. Cooper, M. W. D., Stanek, C. R. & Andersson, D. A. The role of dopant charge state on defect chemistry and grain growth of doped UO_2. *Acta Mater.* **150**, 403–413 (2018).
15. Middleburgh, S. C. et al. Enrichment of chromium at grain boundaries in chromia doped UO_2. *J. Nucl. Mater*. https://doi.org/10.1016/j.jnucmat.2023.154250 (2023).
16. Terricabras, A. J. et al. Performance and properties evolution of near-term accident tolerant fuel: Cr-doped UO_2. *J. Nucl. Mater*. https://doi.org/10.1016/j.jnucmat.2024.155022 (2024).
17. Devillaire, A. et al. First evidence of metallisation circle in a Chromium doped UO_2 pellet submitted to a thermal gradient. *J. Nucl. Mater*. https://doi.org/10.1016/j.jnucmat.2024.155088 (2024).
18. Murphy, G. L. et al. Deconvoluting Cr states in Cr-doped UO_2 nuclear fuels via bulk and single crystal spectroscopic studies. *Nat. Commun*. https://doi.org/10.1038/s41467-023-38109-0 (2023).
19. Riglet-Martial, C. et al. Thermodynamics of chromium in UO_2 fuel: a solubility model. *J. Nucl. Mater.* **447**, 63–72 (2014).
20. Rodríguez-Villagra, N. et al. Dopant effect on the spent fuel matrix dissolution of new advanced fuels: Cr-doped UO_2 and Cr/Al-doped UO_2. *J. Nucl. Mater.* **568**, 153880 (2022).
21. Murphy, G. L. et al. A synchrotron X-ray diffraction and electron microscopy study of vanadium-doped UO_2. *MRS Adv*. https://doi.org/10.1557/s43580-025-01209-8 (2025).
22. Murphy, G. L. et al. The lattice contraction of UO_2 from Cr doping as determined via high resolution synchrotron X-ray powder diffraction. *J. Nucl. Mater.* **595**, 155046 (2024).
23. Murphy, G. L. et al. The role of redox and structure on grain growth in Mn-doped UO_2. *Commun. Mater.* **5**, 274 (2024).
24. Cardinaels, T. et al. Dopant solubility and lattice contraction in gadolinia and gadolinia-chromia doped UO_2 fuels. *J. Nucl. Mater.* **424**, 289–300 (2012).
25. Fullarton, M. L. et al. Structure, properties and formation of $PuCrO_3$ and $PuAlO_3$ of relevance to doped nuclear fuels. *J. Mater. Chem. A* **1**, 14633–14640 (2013).
26. Russell, L. E., Harrison, J. D. L. & Brett, N. H. Perovskite-type compounds based on plutonium. *J. Nucl. Mater.* **2**, 310–320 (1960).
27. Shannon, R. D. Revised effective ionic-radii and systematic studies of interatomic distances in halides and chalcogenides. *Acta Crystallogr. A* **32**, 751–767 (1976).

28. Liu, J. et al. Non-stoichiometric and Subnano-heterogeneous *Ln*-incorporated UO_2: its defect chemistry and thermal oxidation. Preprint at https://doi.org/10.48550/arXiv.2412.03501 (2024).
29. Mieszczynski, C. et al. Microbeam X-ray absorption spectroscopy study of chromium in large-grain uranium dioxide fuel. *J. Phys.-Condens Mat*. https://doi.org/10.1088/0953-8984/26/35/355009 (2014).
30. Hesketh, K., Rossiter, G., Largenton, R. & Puide, M. Burnable poison-doped fuel. *Compr. Nucl. Mater.* **2**, 106–124 (2020).
31. Kegler, P. et al. Chromium doped UO_2-based ceramics: synthesis and characterization of model materials for modern nuclear fuels. *Materials* https://doi.org/10.3390/ma14206160 (2021).
32. Scheinost, A. C. et al. ROBL-II at ESRF: a synchrotron toolbox for actinide research. *J. Synchrotron Radiat.* **28**, 333–349 (2021).
33. Kieffer, J., Valls, V., Blanc, N. & Hennig, C. New tools for calibrating diffraction setups. *Synchrotron Radiat.* **27**, 558–566 (2020).
34. Toby, B. H. & Von Dreele, R. B. GSAS-II: the genesis of a modern open-source all purpose crystallography software package. *J. Appl Crystallogr.* **46**, 544–549 (2013).
35. Kvashnina, K. O. & Scheinost, A. C. A Johann-type X-ray emission spectrometer at the Rossendorf beamline. *J. Synchrotron Radiat.* **23**, 836–841 (2016).
36. Rossberg, A. *Ph.D. Thesis: Application of factor analysis to X-ray absorption spectroscopy for the determination of uranium speciation in solution*, (Technische Universitaet Dresden, Dresden, Germany 2002).
37. Rossberg, A., Reich, T. & Bernhard, G. Complexation of uranium(VI) with protocatechuic acid - application of iterative transformation factor analysis to EXAFS spectroscopy. *Anal. Bioanal. Chem.* **376**, 631–638 (2003).
38. Kraft, D. A software package for sequential quadratic programming. Report No. DFVLR-FB 88-28, 33 (DLR German Aerospace Center—Institute for Flight Mechanics, Köln, Germany, 1988).
39. Chang, C., Xu, W., Chen-Wiegart, Y. C. K., Wang, J. & Yu, D. T. Improving chemical mapping algorithm and visualization in full-field hard X-ray spectroscopic imaging. *Proc. Spie* https://doi.org/10.1117/12.2041109 (2014).
40. Alizadehfanaloo, S. et al. Tracking dynamic structural changes in catalysis by rapid 2D-XANES microscopy. *J. Synchrotron Radiat.* **28**, 1518–1527 (2021).
41. Leinders, G. et al. Refinement of the uranium dispersion corrections from anomalous diffraction. *Appl. Crystallogr.* **57**, 284–295 (2024).
42. Ziegler, J. F., Ziegler, M. D. & Biersack, J. P. SRIM—the stopping and range of ions in matter. *Nucl. Instrum. Meth B* **268**, 1818–1823 (2010).
43. Fitch, A. et al. ID22-the high-resolution powder-diffraction beamline at ESRF. *J. Synchrotron Radiat.* **30**, 1003–1012 (2023).
44. Van Den Hoogenhof, W. W. & De Boer, D. K. G. Glancing-incidence X-ray analysis. *Spectrochim. Acta Part B At. Spectrosc.* **48**, 277–284 (1993).
45. Ohmichi, T., Fukushima, S., Maeda, A. & Watanabe, H. On the relation between lattice-parameter and O/M ratio for uranium-dioxide trivalent rare-earth-oxide solid-solution. *J. Nucl. Mater.* **102**, 40–46 (1981).
46. Prieur, D. et al. Aliovalent cation substitution in UO_2: electronic and Local Structures of $U_{1-y}La_yO_{2\pm x}$ Solid Solutions. *Inorg. Chem.* **57**, 1535–1544 (2018).
47. Vinograd, V. L., Bukaemskiy, A. A., Modolo, G., Deissmann, G. & Bosbach, D. Thermodynamic and structural modelling of non-stoichiometric *Ln*-doped UO_2 solid solutions *Ln* = {La, Pr, Nd, Gd}. *Front. Chem*. https://doi.org/10.3389/fchem.2021.705024 (2021).
48. Bès, R. et al. Charge compensation mechanisms in $U_{1-x}Gd_xO_2$ and $Th_{1-x}Gd_xO_2$ studied by X-ray absorption spectroscopy. *J. Nucl. Mater.* **489**, 9–21 (2017).
49. Mao, P. V. et al. Crystal structure of $U_{1-y}Ln_yO_{2-x}$ (*Ln*= Gd, Er) solid solution. *J. Nucl. Mater* https://doi.org/10.1016/j.jnucmat.2021.153189 (2021).
50. Herrero et al. Charge compensation mechanisms in Nd-doped UO_2 samples for stoichiometric and hypo-stoichiometric conditions: lack of miscibility gap. *J. Nucl. Mater*. https://doi.org/10.1016/j.jnucmat.2020.152276 (2020).
51. Smith, H. et al. Fabrication, defect chemistry and microstructure of Mn-doped UO_2. *Sci. Rep.-Uk* https://doi.org/10.1038/s41598-023-50676-2 (2024).
52. Kvashnina, K. O., Butorin, S. M., Martin, P. & Glatzel, P. Chemical state of complex uranium oxides. *Phys. Rev. Lett*. https://doi.org/10.1103/PhysRevLett.111.253002 (2013).
53. Bauer, M. HERFD-XAS and valence-to-core-XES: new tools to push the limits in research with hard X-rays? *Phys. Chem. Chem. Phys.* **16**, 13827–13837 (2014).
54. Pocol, V. et al. Some polynuclear coordination compounds precursors of chromites - Synthesis, physicochemical characterization and thermal stability. *J. Therm. Anal. Calorim.* **55**, 143–154 (1999).
55. Fergus, J. W. Lanthanum chromite-based materials for solid oxide fuel cell interconnects. *Solid State Ion.* **171**, 1–15 (2004).
56. Townsend, L. T. et al. Analysis of the structure of heavy ion irradiated $LaFeO_3$ using grazing angle X-ray absorption spectroscopy. *Inorg. Chem.* **63**, 8531–8536 (2024).
57. Kleykamp, H. The chemical-state of the fission-products in oxide fuels. *J. Nucl. Mater.* **131**, 221–246 (1985).
58. Kleykamp, H. The chemical-state of fission-products in oxide fuels at different stages of the nuclear-fuel cycle. *Nucl. Technol.* **80**, 412–422 (1988).
59. Zhang, L., Solomon, J. M., Asta, M. & Navrotsky, A. A combined calorimetric and computational study of the energetics of rare earth substituted UO_2 systems. *Acta Mater* **97**, 191–198 (2015).
60. Goldschmidt, V. M. The laws of crystal chemistry. *Naturwissenschaften* **14**, 477–485 (1926).
61. Momma, K. & Izumi, F. VESTA 3 for three-dimensional visualization of crystal, volumetric and morphology data. *J. Appl. Crystallogr.* **44**, 1272–1276 (2011).

Acknowledgements

The authors are grateful to the funding and support from the Helmholtz Graduate School for Energy and Climate Research (HITEC) at Forschungszentrum Juelich GmbH. We acknowledge the European Synchrotron Radiation Facility (ESRF) and Helmholtz-Zentrum Dresden-Rossendorf for provision of synchrotron radiation facilities under proposal numbers A20-1-868 and CH-7424. The authors are grateful for assistance with ion irradiations from Prof. Christina Trautmann. The authors are grateful for support from the from the German Federal Ministry of Education and Research (BMBF), Project No. 02NUK088A.

Author contributions

The project was conceived and developed by Gabriel L. Murphy. Research methodology, experimental planning and formal analysis were conducted by Daniil Shirokiy and Gabriel L. Murphy. Synthesis of materials was done by Daniil Shirokiy, Andrey Bukaemskiy and Maximillian Henkes. Synchrotron X-Ray diffraction was performed by Christoph Hennig, Daniil Shirokiy, Gabriel L. Murphy and Julien Marquardt. X-ray absorption spectroscopy measurements were performed by Kristina O. Kvashnina, Elena Bazarkina, Daniil Shirokiy, Julien Marquardt and Gabriel L. Murphy. Ion irradiation was performed by Julien Marquardt. Stopping range of ions in matter calculations were performed by Daniil Shirokiy and Andrew Ryan. Grazing incidence X-Ray diffraction was performed by Andrew Fitch, Christoph Hennig, Daniil Shirokiy, Mara McCleary and Gabriel L. Murphy. Electron microscopy imaging was performed by Martina Klinkenberg, Murat Güngör and Daniil

Shirokiy. Manuscript writing, reviewing and editing was performed by Daniil Shirokiy, Gabriel L. Murphy and Dirk Bosbach with input from all authors.

Funding
Open Access funding enabled and organized by Projekt DEAL.

Competing interests
The authors declare no competing interests.

Additional information
Supplementary information The online version contains supplementary material available at https://doi.org/10.1038/s41529-026-00752-5.

Correspondence and requests for materials should be addressed to Daniil Shirokiy or Gabriel L. Murphy.